REVISTA INTERDISCIPLINAR DE PESQUISA EM ENGENHARIA

CILAMCE 2016

XXXVII IBERIAN LATIN AMERICAN CONGRESS ON COMPUTATIONAL METHODS IN ENGINEERING
BRASÍLIA - DF - BRAZIL

INCORPORATION OF BACK-PRESSURE EFFECTS IN THE MODELING OF THE PISTON RING/CYLINDER LINER

Alfredo Jaramillo Palma[(a)]

ajaramillopalma@icmc.usp.br

Hugo Checo Silva[(a)]

hcheco@icmc.usp.br

Gustavo Carlos Buscaglia[(a)]

gustavo.buscaglia@icmc.usp.br

(a) Universidade de São Paulo

13560-970, São Carlos, São Paulo, Brazil

Abstract. *The piston ring/cylinder liner system is responsible for about 5% of the energy lose due to friction in a passenger car (Holmberg et al., 2012). Consequently, automotive industry and academy have made efforts seeking for designs that diminish both friction and wear. During the last year, several numerical and experimental studies have shown that texturization can have favorable or detrimental effects on the tribological characteristics of lubricated mechanisms. However, few studies have included the effects of the gas pressure in the combustion chamber, which variates rapidly in the compression stroke and can reach values as high as 60[atm]. Reynolds equation with zero-pressure Dirichlet conditions is mainly adopted in numerical works along with Elrod-Adams cavitation model. This cavitation model only admits a constant cavitation pressure, in spite it is known that cavitation pressure can variate according to the operational conditions (Shen et al., 2013). This work is devoted to the study of the effects that the combustion chamber pressure can have on both the mechanical dynamic of the rings and the cavitation pressure* p_{cav}.

Keywords: *Hydrodynamic lubrication; Friction force; Back-pressure effects; Elrod-Adams model*

1 INTRODUCTION

The numerical modeling of the piston ring/cylinder liner (PRCL) is a challenging problem that requires to consider different aspects of design and operation conditions such as surface texturing, pressure boundary conditions, forces developed, among others. Particularly, the gas pressure in the combustion chamber varies significantly in the transition from compression to power stroke ($\sim$ from 1 to 60 atm), which may have important effects on the rings dynamics.

Surface texturing is a design technique that implies the presence of many convergent-divergent zones that may lead to several non-connected pressurized regions. Between these pressurized regions, tensile stresses (negative pressures) lead to a rupture in the film continuity. Such physical phenomenon is known as cavitation and, when textures effects are considered within Reynolds equation, implies the use of a mass-conservative algorithm like the Elrod-Adams cavitation model (Ausas et al., 2007; Qiu et al., 2009).

Using Elrod-Adams model, Checo et al. (2014) found numerically that traveling textures (placed on the moving liner) may have beneficial effects only for moderate to high conformity between the cylinder and the rings, reducing up to 73% the friction coefficient. This is in line with previous numerical findings of Dobrica et al. (2010) within a stationary regime, and with the results obtained by Gadeschi et al. (2012) by means of a non-conservative algorithm, among other numerical works. However, those numerical studies have not considered the back-pressure effects. On the other hand, Morris, Leighton, et al. (2014), Morris, Rahmani, et al. (2015) and Usman et al. (2016) have included back-pressure effects by means of a non-conservative cavitation model.

In this work, we propose an extension of the Elrod-Adams cavitation model along Reynolds equation to consider back-pressure effects and cavitation in a mass-conservative fashion. That extension imposes a constrain on the hydrodynamical pressure, meaning that the hydrodynamical pressure must be point-wisely greater or equal that a scalar field called *cavitation pressure*. The cavitation pressure is modeled as a function of the saturation variable θ. The details of that modeling are presented in Section 'Mathematical Modeling'. In Section 'Discretization' the discrete model and the numerical algorithm are presented. In Section 'Numerical experiments' the results of first numerical test are shown. Finally, in the last section some conclusions and future research are commented.

2 MATHEMATICAL MODELING

Consider the computational domain $\Omega = [0, L] \times [0, B]$, with boundary Γ, and denote as $\Gamma_\ell = \{[0, x_2],\, x_2 \in [0, B]\}$, $\Gamma_r = \{(1, x_2),\, x_2 \in [0, B]\}$, the left and right sides respectively. Ω represents the region just under the ring, so its left side is considered to be at $x_1 = 0$ and its right side at $x_1 = L$. The relative velocity between the surfaces is denoted by U. The unknowns of the problem are: the hydrodynamic pressure $p(x_1, x_2, t)$, the saturation variable $\theta(x_1, x_2, t)$ and the cavitation pressure $p_{cav}(x_1, x_2, t)$.

The Elrod-Adams model incorporates into a single formulation the Reynolds equation and the Jacobson-Floberg-Olsson boundary conditions for the rupture and reformation points. The Reynolds equation along with the equation for p_{cav} and the boundary conditions reads (for all

time t)

$$\text{div}\left(\frac{h^3}{12\,\mu}\nabla p\right) - \frac{U}{2}\nabla(h\theta) = \frac{\partial h\theta}{\partial t}, \qquad \text{on } \Omega, \tag{1}$$

$$p \geq p_{cav},\ 0 \leq \theta \leq 1, \qquad \text{on } \Omega, \tag{2}$$

$$p(x_1, x_2, t) = 0, \qquad \text{on } \Gamma_\ell, \tag{3}$$

$$p(x_1, x_2, t) = p_{cc}(t), \qquad \text{on } \Gamma_r, \tag{4}$$

$$\theta(x_1, x_2, t) = \theta_{feed}, \qquad \text{on } \Gamma_\ell \text{ if } S > 0 \text{ or } \Gamma_r \text{ if } S < 0, \tag{5}$$

where θ is a saturation variable such that $p(x_1, x_2, t) = p_{cav}(x_1, x_2, t)$ if and only if $\theta(x_1, x_2) = 1$, on Ω. The cavitation pressure is given by the operator T (for each time t):

$$\begin{array}{rccc} T: & L^\infty(\Omega) & \mapsto & L^\infty(\Omega) \\ & \theta & \mapsto & p_{cav} = T\theta. \end{array}$$

Let us denote $\Lambda^t = \{(x_1, x_2) \in \Omega : \theta(x_1, x_2, t) < 1\}$, and by Λ_r^t the union of the connected components of Λ^t such that $\Lambda^t \cap \Gamma_r \neq \emptyset$ (observe that it would happen that $|\Lambda_r^t| = 0$). With this, in the present work T is defined as

$$(T\theta)(x_1, x_2) = \begin{cases} p_{cc}(t) & \text{if } (x_1, x_2) \in \Lambda_r^t \\ 0 & \text{if } (x_1, x_2) \notin \Lambda_r^t \end{cases}. \tag{6}$$

Figure 1 illustrates the action of the operator T used in the examples exposed in this work.

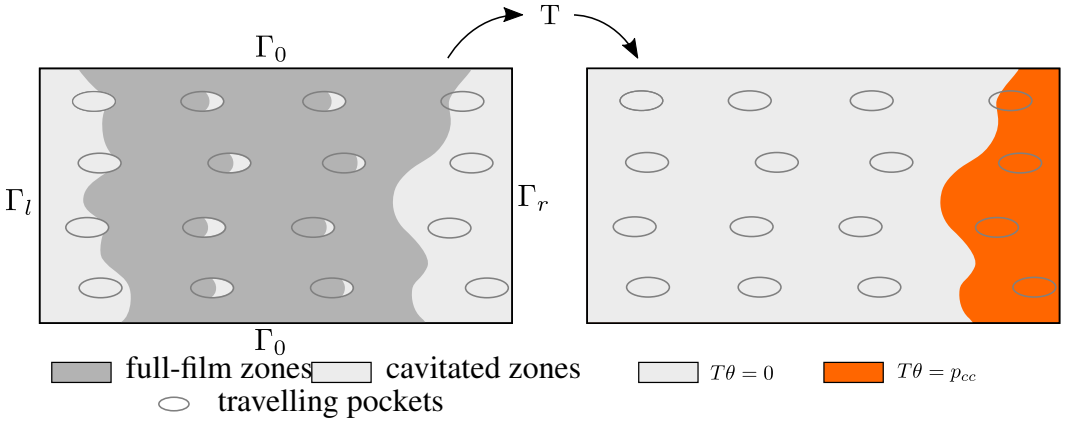

Figure 1: Example of the cavitation pressure develop from the saturation variable through the operator T.

3 DISCRETIZATION

We divide Ω in $N_{x_1} \times N_{x_2}$ cells (using half-cells at the boundaries) and denote by I the set of indexes of the cells corresponding to internal nodes (where the unknowns are placed). A finite volumes scheme for equation (1) is used, for this, the x_1 flux component going from node $(i-1, j)$ to node (i, j) can be discretized by

$$-\frac{h^3}{12\mu}\frac{\partial p}{\partial x_1} + \frac{U}{2}h\theta \approx -\frac{1}{12\,\mu}\frac{(h_{i-1,j}^n)^3 + (h_{i,j}^n)^3}{2}\frac{p_{i,j}^n - p_{i-1,j}^n}{\Delta x_1} + \frac{U}{2}h_{i-1,j}^n\theta_{i-1,j}^n, \tag{7}$$

where an upwind scheme is used for the Couette term. Balancing the fluxes on each cell (for the x_2 components only diffusive terms need to be included) and discretizing time along an implicit scheme for the temporal term $\frac{\partial h\theta}{\partial t}$ we get to a system of equations that reads, for each $(i,j) \in I$,

$$a^{00}_{i,j}\, p^n_{i,j} + e^{00}_{i,j}\, \theta^n_{i,j} = C_{i,j}(\boldsymbol{p}^n, \boldsymbol{\theta}^n), \tag{8}$$

$$\boldsymbol{p}^n_{cav} = T(\boldsymbol{\theta}), \tag{9}$$

$$p^n_{i,j} \geq p^n_{cav;i,j}, \tag{10}$$

$$0 \leq \theta^n_{i,j} \leq 1, \tag{11}$$

$$(p^n_{i,j} - p^n_{cav;i,j})(1 - \theta^n_{i,j}) = 0, \tag{12}$$

where

$$C_{i,j}(\boldsymbol{p}^n, \boldsymbol{\theta}^n) = -\, a^{-0}_{i,j} p^n_{i-1,j} - a^{+0}_{i,j} p^n_{i+1,j} - a^{0+}_{i,j} p^n_{i,j+1} - a^{0-}_{i,j} p^n_{i,j-1} - e^{-0}_{i,j} \theta^n_{i-1,j} + f^n_i, \tag{13}$$

with

$$a^{00}_{i,j} = s^n_{i+1,j} + s^n_{i-1,j} + (\Delta x_1/\Delta x_2)^2 \left(s^n_{i,j+1} + s^n_{i,j-1}\right), \quad e^{00}_{i,j} = (S\Delta x_1 + 2\Delta t/\Delta x)\, h^n_{i,j},$$
$$a^{+0}_{i,j} = -s^n_{i+1,j}, \quad a^{-0}_{i,j} = -s^n_{i-1,j},$$
$$a^{0-}_{i,j} = -(\Delta x_1/\Delta x_2)^2\, s^n_{i,j-1}, \quad a^{0+}_{i,j} = -(\Delta x_1/\Delta x_2)^2\, s^n_{i,j+1},$$
$$e^{-0}_{i,j} = -S\Delta x_1\, h^n_{i-1,j}, \quad s^n_{i\pm1,j\pm1} = \tfrac{1}{6\,\mu}\left((h^n_{i,j})^3 + (h^n_{i\pm1,j\pm1})^3\right).$$
$$f^n_i = 2\Delta x/\Delta t\, h^{n-1}_{i,j}\theta^{n-1}_{i,j}$$

Please notice that $s^n_{i\pm1,j\pm1} \geq 0$, and so $a^{00}_{i,j}, e^{00}_{i,j} \geq 0$, and each term $a^{+0}_{i,j}$, $a^{-0}_{i,j}$, $a^{0+}_{i,j}$, $a^{0-}_{i,j}$, $e^{-0}_{i,j}$ is non-positive, and thus $C_{i,j}(\boldsymbol{p}^n, \boldsymbol{\theta}^n) \geq 0$. This type of discrete system was already studied by Alt (1980) and by Marini et al. (1986). In the former work, the author proposed an elegant fixed-point iterative method to solve the system, while in the later work it is shown the convergence of resulting sequence to the solution of the discrete system in the case $T \equiv 0$.

3.1 Well posedness of the discrete system

Fixed-point framework. To relax the notation, we omit the dependence of $C_{i,j}$ on $(\boldsymbol{p}^n, \boldsymbol{\theta}^n)$ and the time step supra-index n. Following the development made by Alt (1980) and Marini et al. (1986), we write the system of equations (8)-(12) as a fixed-point problem by defining the operator B_T, acting on the pair $(\boldsymbol{p}, \boldsymbol{\theta})$, as

$$(B_T(\boldsymbol{p},\boldsymbol{\theta}))_{i,j} = \begin{cases} \left(\frac{1}{a^{00}_{i,j}}\left(C_{i,j} - e^{00}_{i,j}\right),\, 1\right) & \text{if } \; C_{i,j} - e^{00}_{i,j} \geq a^{00}_{i,j}\,(T\boldsymbol{\theta})_{i,j} \\ \left((T\boldsymbol{\theta})_{i,j},\, \frac{1}{e^{00}_{i,j}}\left(C_{i,j} - a^{00}_{i,j}\,(T\boldsymbol{\theta})_{i,j}\right)\right) & \text{if } \; C_{i,j} - e^{00}_{i,j} < a^{00}_{i,j}\,(T\boldsymbol{\theta})_{i,j} \end{cases},$$

for each cell $(i,j) \in I$. Allowing us to write Eq. (8) as the fixed-point equation

$$B_T(\boldsymbol{p},\boldsymbol{\theta}) = (\boldsymbol{p},\boldsymbol{\theta}). \tag{14}$$

Let us divide the set I as $I = I_0 \overset{\circ}{\cup} I_r$, where I_r is the subset of cells in the region Λ^t_r and $I_0 = I \backslash I_r$. Please observe that a solution to Eq. (14) accomplishes automatically the restrictions

(9), (10) and (12) for any $(i,j) \in I$. However, the only immediate property of $\theta_{i,j}$ is that $\theta_{i,j} \leq 1$. To analyze the sign of $\theta_{i,j}$, observe that

$$C_{i,j}(\boldsymbol{p},\boldsymbol{\theta}) - a^{00}_{i,j}(T\boldsymbol{\theta})_{i,j} = f_{i,j} + S\Delta x_1 h_{i-1,j}\theta_{i-1,j} + \Delta''_{i,j}, \tag{15}$$

where

$$\begin{aligned}\Delta''_{i,j} = {} & s_{i-1,j}\left(p_{i-1,j} - (T\boldsymbol{\theta})_{i,j}\right) + s_{i+1,j}\left(p_{i+1,j} - (T\boldsymbol{\theta})_{i,j}\right) + \\ & + q^2\left\{s_{i,j-1}\left(p_{i,j-1} - (T\boldsymbol{\theta})_{i,j}\right) + s_{i,j+1}\left(p_{i,j+1} - (T\boldsymbol{\theta})_{i,j}\right)\right\}.\end{aligned} \tag{16}$$

Thus, $\theta_{i,j}$ can be negative on the cells in I_r such that some of its neighbors belongs to the set I_0. To overcome this issue the discrete version of the operator T is defined as follows

$$(T\boldsymbol{\theta})_{i,j} = \begin{cases} p_{cc}(t) & \text{if } (i,j) \in I_r \cup \partial I_r \\ 0 & \text{if } (i,j) \in I_0 \setminus \partial I_r \end{cases}, \tag{17}$$

where $\partial I_r = \{(i,j) \in I_0 : V(i,j) \cap I_r \neq \emptyset\}$ and $V(i,j) = \{(i \pm 1, j), (i, j \pm 1)\}$ (horizontal and vertical neighbors of (i,j)). Figure 2 illustrates the action of the discrete operator T.

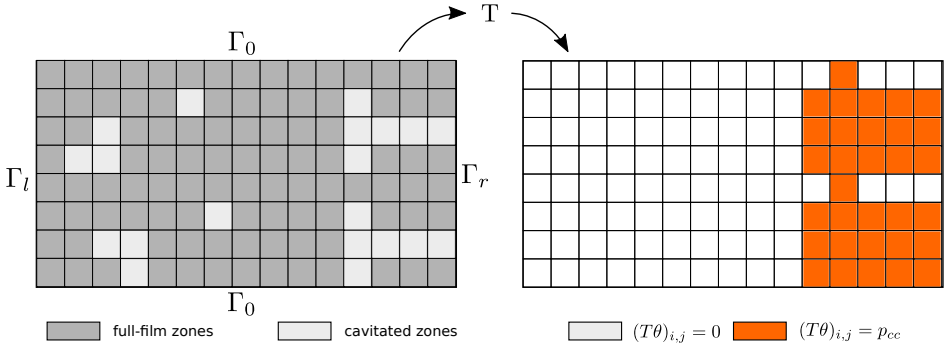

Figure 2: Illustration of the action of the discrete operator T. Notice that $(T\theta)_{i,j} = p_{cc}$ also on the neighbors of I_r.

Existence. Let us define the iterative process

$$\left(\boldsymbol{p}^{k+1}, \boldsymbol{\theta}^{k+1}\right) = B_T\left(\boldsymbol{p}^k, \boldsymbol{\theta}^k\right), \tag{18}$$

starting from some initial guess $(\boldsymbol{p}^0, \boldsymbol{\theta}^0)$. The convergence of the sequence defined by Eq. (18) to a solution of Eq. (14) is proved by Marini et al. (1986) based in the monotonicity of the operator B_0 (i.e., if $(\boldsymbol{p}_1, \boldsymbol{\theta}_1) \geq (\boldsymbol{p}_2, \boldsymbol{\theta}_2)$, by components, then $B_0(\boldsymbol{p}_1, \boldsymbol{\theta}_1) \geq B_0(\boldsymbol{p}_2, \boldsymbol{\theta}_2)$). On the other hand, for the operator T defined in (6), let us take some vector $\boldsymbol{p}$ and two vectors $\boldsymbol{\theta}_1$, $\boldsymbol{\theta}_2$, with $\boldsymbol{\theta}_1 > \boldsymbol{\theta}_2$, then, it can be seen that $\left(B_0(\boldsymbol{p}, \boldsymbol{\theta}_1)\right)_{i,j} \geq \left(B_0(\boldsymbol{p}, \boldsymbol{\theta}_2)\right)_{i,j}$ on the cells where $C_{i,j}(\boldsymbol{p}, \boldsymbol{\theta}_1) - e^{00}_{i,j} \geq a^{00}_{i,j}\left(T\boldsymbol{\theta}_1\right)_{i,j}$. However, on the cells where $C_{i,j}(\boldsymbol{p}, \boldsymbol{\theta}_1) - e^{00}_{i,j} < a^{00}_{i,j}\left(T\boldsymbol{\theta}_1\right)_{i,j}$ nothing can be assured, in fact, simple examples can be constructed where $\left(B_0(\boldsymbol{p}, \boldsymbol{\theta}_1)\right)_{i,j} < \left(B_0(\boldsymbol{p}, \boldsymbol{\theta}_2)\right)_{i,j}$ on those cells. Thus, for the operator T defined here the monotonicity is lost, and so the study the well-posedness of the discrete system is harder.

4 Numerical experiments

The algorithm used in this work for the numerical tests is shown in Table 1. That algorithm is a natural extension of the one described in Marini et al. (1986). For all the tests the upper surface is in rest while the lower surface is moving to the right with velocity $U = 10$ m/s.

Table 1: Adaptation of the numerical algorithm presented in Marini et al. (1986) for the non trivial operator T.

Algorithm 1: Numerical algorithm for solving the system (8)-(12).

Input: h: gap function, p^0, θ^0: initial guess
begin
  $k = 1$;
  $p^1 = p^0$; $\theta^1 = \theta^0$;
  while *change* $>$ *tol* **do**
    compute $p^k_{cav} = T(\theta^k)$;
    for $i = 1 \dots N_{x_1}$, $j = 1 \dots N_{x_2}$ **do**
      if $\left(C_{i,j} - e^{00}_{i,j}\right)/a^{00}_{i,j} \geq p^k_{cav;i,j}$ **then**
        $p^k_{i,j} = (C_{i,j} - e^{00}_{i,j})/a^{00}_{i,j}$;
        $\theta^k_{i,j} = 1$;
        else
          $\theta^k_{i,j} = (C_{i,j} - a^{00}_{i,j}\, p^k_{cav;i,j})/e^{00}_{i,j}$;
          $p^k_{i,j} = p^k_{cav;i,j}$;
        end
      end
      update arrays a and e;
    end
    compute $change$;
    $p^{k+1} = p^k$; $\theta^{k+1} = \theta^k$;
    $k = k + 1$;
  end
  return p^{k+1}, θ^{k+1}, $p^{k+1}_{cav} \equiv T(\theta^{k+1})$;
end

For all cases the length (on x_1) of the pad is fixed as L = 1 mm, and the viscosity of the lubricant oil is set to $\mu = 4 \times 10^{-3}$ Pa·s.

One-dimensional tests.

Test 1

Due to the positive mechanical pressure present at the combustion chamber there would happen leaks of oil/gas through the ring-liner gap, such undesirable effect is known as *blow-by* (Wang et al., 2013). Here we solve stationary cases taking a fixed value for p_{cc} with the next geometry

$$h(x_1) = 1[\mu m] + \frac{\left(x_1 - 0.5 \times 10^{-3}[m]\right)^2}{2R}.$$

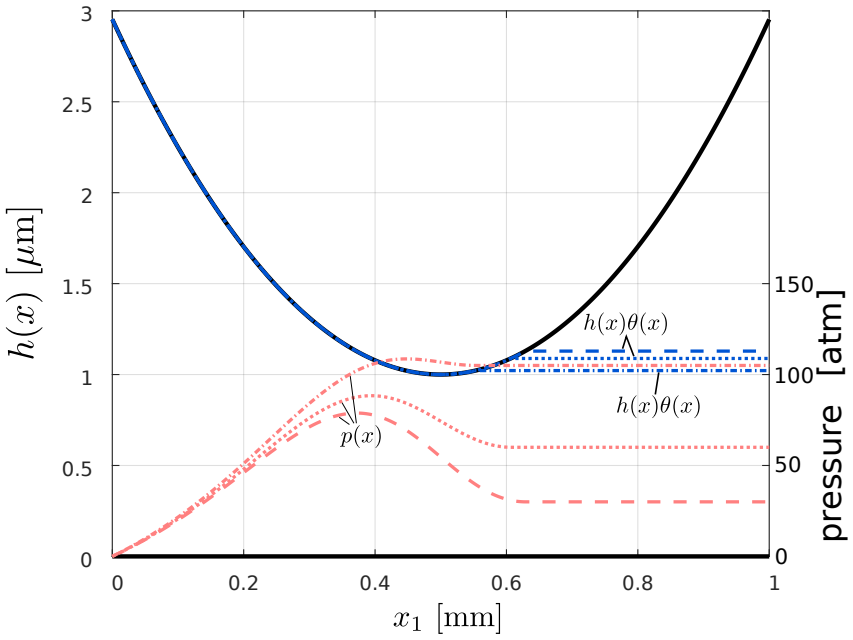

Figure 3: Results for Test 1. The dashed lines, dotted lines and dotted-dashed lines correspond to $p_{cc} = 30$, 60, and 105 atm respectively. $h\theta$ is the fluid height at each point.

R [mm]	8	16	32	64	128
p^*_{cc} [atm]	31.5	55.3	85.5	106.9	109.6

Table 2: Values of p_{cc} from which blow-by occurs for different values of R.

Figure 3 shows the resulting pressure fields for $R = 64$ mm, $p_{cc}(t) \equiv 30,\ 60$, and 105 atm.

Notice that the pressure profile adapts to the right boundary condition. Also, taking a higher value for p_{cc} has the effect of moving the separation point to the left (for this particular geometry the separation point is always placed at the left of $x = 0.5$ mm). For $p_{cc} = 30$ atm, the separation point is placed at $x = 0.628$ mm, for $p_{cc} = 60$ atm it is placed at $x = 0.605$ mm, and for $p_{cc} = 105$ atm it is placed at $x = 0.552$ mm. The blow-by effect for $R = 32$ mm occurs for $p_{cc} \geq 106.9$ atm. Table 2 shows the critical value of p_{cc} for which blow-by occurs when changing R. It can be observed that rings with a higher conformity (higher R) are able to support higher values of p_{cc} without fluid leakage (of course the critical value of p_{cc} also depends on the minimum value of $h(x)$, which in these cases is fixed to 1 micron).

Test 2

Here a stationary case is solved. The geometry is set as

$$h(x_1) = 1{\times}10^{-6}[m] + \left[0.45(10^{-3}[m] - x_1) + 0.4\,x_1\right]{\times}10^{-3}\cos(4\pi\,x_1{\times}10^{3}[m^{-1}]) + 5\,x_1{\times}10^{-5}),$$

along with the inlet condition $\theta_\ell = 1$ (fully-flooded condition) and $p_{cc} = 5$ atm.

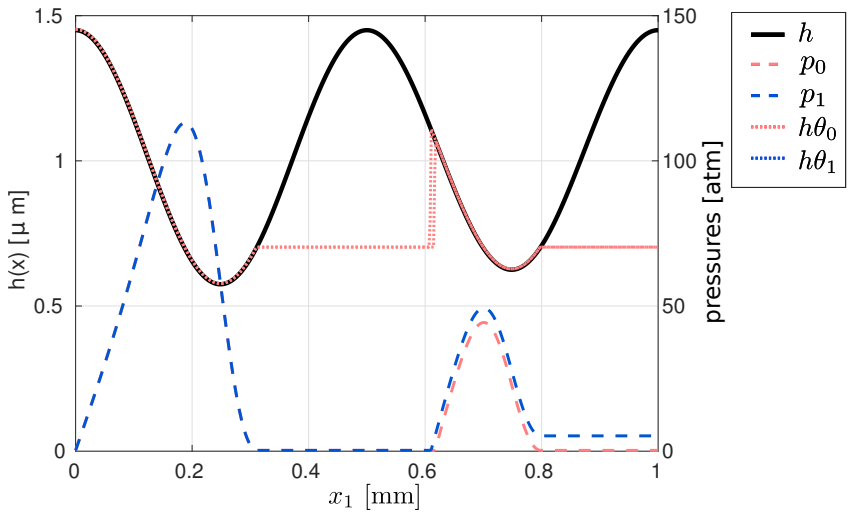

Figure 4: Resulting fields for Test 2. p_0 is the resulting pressure for $p_{cc} = 0$ atm and p_1 is the resulting pressure for $p_{cc} = 5$ atm. $h\theta$ is the fluid height at each point.

The results for this case are shown in Fig. 4, where p_0 is the resulting pressure for $p_{cc} = 0$ atm and p_1 is the resulting pressure for $p_{cc} = 5$ atm. Focusing on p_1, please observe that two partial-film zones (i.e., $\theta < 1$) are formed, one near the center of the domain with cavitation pressure equal to 0 atm, and a second region where the cavitation pressure is equal to $p_{cc} = 5$ atm. On the left pressurized region both p_0 and p_1 are equal, while on the right region there is a difference of 8% in the predicted force (integral of the pressure on the domain) applied by the pressure field on the surfaces. Notice that a part of this difference corresponds to a bigger pressure build-up due to a higher pressure on the right separation boundary ($x_1 \approx 0.8$ mm).

Test 3

In this case, the gap between the two surfaces reads

$$h(x_1, t) = Z(t) + h_p(x_1) = Z(t) + \frac{(x_1 - 0.5 \times 10^{-3}[m])^2}{2R}, \tag{19}$$

where the minimum clearance $Z(t)$ is found by solving the newton equation for the ring (by means of a Newmark scheme), which is supposed to have a mass density of $m = 4.8 \times 10^{-2}$ kg/m and a curvature equal to $R = 32$ mm.

The forces acting on the ring along the x_3-axis are listed next

- $\boldsymbol{W^{ps}}$: the pre-stress elastic response to deformation (here taken equal to 40 N/m);
- $\boldsymbol{W^{gp}}$, the gas-pressure force originated from the leakage of the chamber pressure ($p_{cc}(t)$) through the gap that exists between the ring and the piston, modeled by

$$W^{gp}(t) = -0.9\, p_{cc}(t);$$

- $\boldsymbol{W^{h}}$: the force originated from the hydrodynamical pressure $p(x_1, x_2, t)$ that develops in the oil film between the ring and the cylinder, given by $W^h = \int_\alpha^\beta p\, dx_1$, where $[\alpha, \beta] \subset [0, 1]$ is the region where the fluid is not *separated* from the ring. Notice that inside $[\alpha, \beta]$ cavitated regions ($0 \leq \theta < 1$) could develop;

- $\boldsymbol{W^m}$: the force developed due to the mechanical pressure of the chamber under the ring, computed as $W^m = \int_\beta^1 p_{cc}\, dx$.

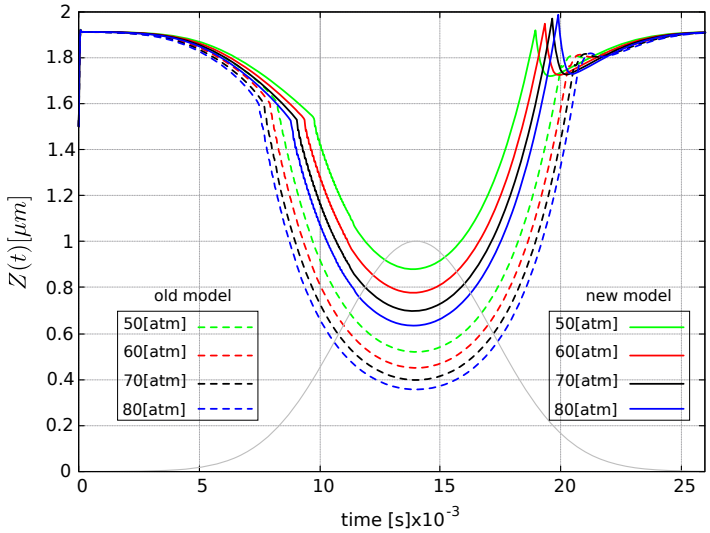

Figure 5: Pad position $Z(t)$ versus time for several explosion amplitudes A. The results of the proposed model are presented in continuous lines, while the results for the old model are presented in dashed lines. The Gaussian-like curve represents the normalized chamber pressure in time.

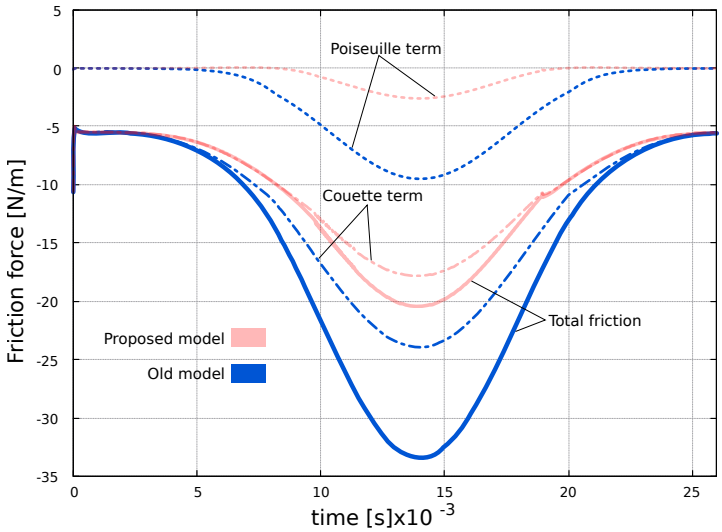

Figure 6: Friction force versus time for an explosion amplitude $A = 50$ atm. The Couette term. The results of the proposed model are presented in continuous lines, while the results for the old model are presented in dashed lines.

In this case we address the effects that an explosion in the combustion chamber may have on the ring dynamics of a cylinder in an engine car. Such explosion is modeled by a Gaussian pulse, i.e.,

$$p_{cc}(t) = A \cdot \exp\left(-2.0 \times 10^5[s^{-2}] \cdot (t - 0.014[s])^2\right),$$

with a time duration of about 20 ms. The resulting ring position $Z(t)$ given by the model proposed here are compared in Fig. 5 with the ones given by the *old model*, i.e., solving Reynolds

equation along the Elrod-Adams cavitation model with heterogeneous zero-pressure conditions. Also, the results for friction given by both models are compared in Fig. 6 where the total friction and its two terms (integrated along the domain) are shown: the Couette term $-\mu U/h$ and the Poiseuille term $-\frac{h}{2}\frac{\partial p}{\partial x}$ (the pressure term is not included as the lower surface is flat). Notice that for both the ring position in time and transient friction the differences between the new and the old model are important.

Two-dimensional tests. Here the ring width is set as $B = 0.1$ mm. Stationary cases are con-

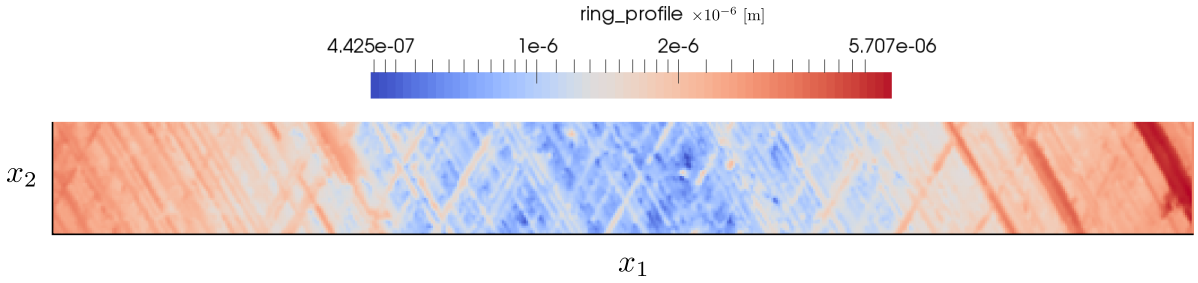

Figure 7: Gap function $h(x_1, x_2)$ considered in the 2-dimensional cases.

sidered, so the r.h.s. of Equation (1) is null. The gap between the ring and the cylinder is taken as

$$h(x_1, x_2) = 1[\mu m] + h_p(x_1) + h_{text}(x_1, x_2), \tag{20}$$

where h_p is taken as in Eq. (19). The texture field h_{text} represents a typical surface-roughness obtained by a honing process. The resulting scalar field $h(x_1, x_2)$ is shown in Figure 7.

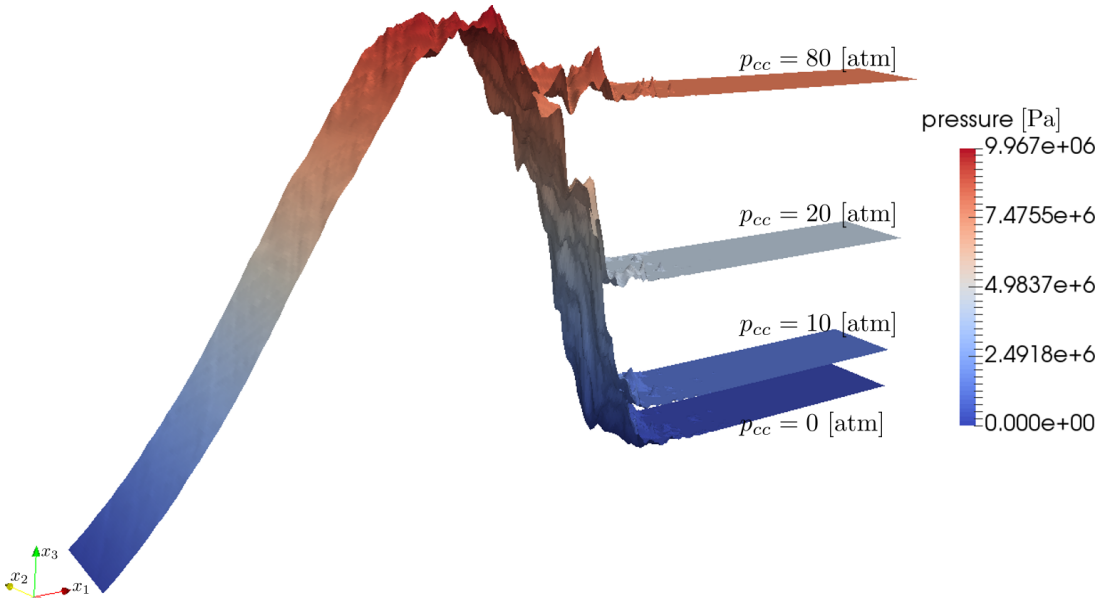

Figure 8: Pressure profiles for each value of p_{cc} including surface roughness.

A blow-by test is made for $p_{cc} = 0, 10, 40, 80$ and 100 atm. The results including surface roughness are compared with those of smooth surface (not considering the last term in Eq. 20). Figure 8 shows the pressure profiles obtained for each case. Figure 9 shows the separation

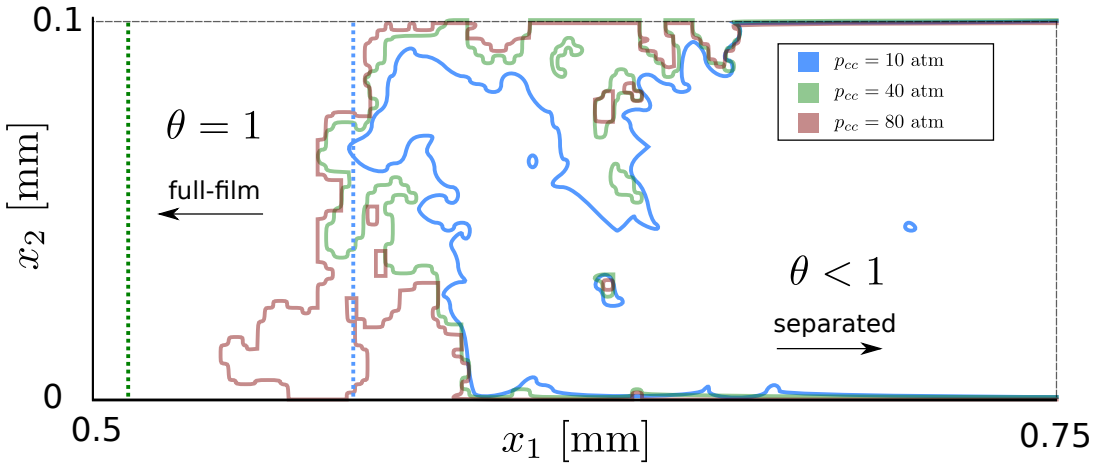

Figure 9: Separation boundaries for each value of p_{cc} considering surface roughness (continuous lines) and without considering surface roughness (dashed lines).

limits for the different values of p_{cc} considered. Notice how the separation boundary (shown in continues lines) advance when augmenting p_{cc}. It is remarkable that for smooth surfaces (dashed-lines) the separation boundary closer to $x_1 = 0.5$ mm. In fact, the smooth surface present blow-by for values of p_{cc} higher than 63 atm, while the surface including roughness showed blow-by for values of p_{cc} higher than 100 atm.

5 Conclusions and forthcoming research

The proposed model is an attempt to identify separation of fluid-film boundaries when heterogeneous boundary conditions are impose for the hydrodynamical pressure.

The well-posedness of the mathematical problem and the convergence of the numerical algorithm here proposed are research topics to be studied next. Another research topic is the modeling of the interaction between cavitated zones developed at different cavitation pressures. This is a challenging problem that would allow to include textures on both the lower and upper surfaces. For this, Rayleigh-Plesset equation will be studied in order to model the operator T in a more physically realistic way.

ACKNOWLEDGEMENTS

The authors acknowledge the financial support of CAPES (grant PROEX-8434433/D), FAPESP (2011/24147-5) and CNPq (grant 447904/2011-0).

REFERENCES

Alt, H. W. 1980. Numerical solution of steady-state porous flow free boundary problems. *Numer. Math.* vol. 36.n. 1, pp. 73–98.

Ausas, R. et al. 2007. The impact of the Cavitation model in the Analysis of Micro-Textured Lubricated Journal bearings. *ASME J. Tribol.* vol. 129.n. 4, pp. 868–875.

Checo, H. M. et al. 2014. Moving textures: Simulation of a ring sliding on a textured liner. *Tribol. Int.* vol. 72, pp. 131–142.

Dobrica, M. B. et al. 2010. Optimizing surface texture for hydrodynamic lubricated contacts using a mass-conserving numerical approach. *Proc. IMechE* vol. 224.n. 8, pp. 737–750.

Gadeschi, G. B., K. Backhaus, & G. Knoll. 2012. Numerical Analysis of Laser-Textured Piston-Rings in the Hydrodynamic Lubrication Regime. *ASME J. Tribol.* vol. 134.n. 4, pp. 1–8.

Holmberg, K., P. Andersson, & A. Erdemir. 2012. Global energy consumption due to friction in passenger cars. *Tribol. Int.* vol. 47, pp. 221–234.

Marini, L. D. & P. Pietra. 1986. Fixed-point Algorithms for Stationary Flow in Porous Media. *Comput. Methods Appl. Mech. Eng.* vol. 56.n. 1, pp. 17–45.

Morris, N., M. Leighton, et al. 2014. Combined numerical and experimental investigation of the micro-hydrodynamics of chevron-based textured patterns influencing conjunctional friction of sliding contacts. *Proc. Inst. Mech. Eng. Part J J. Eng. Tribol.* n. 4.

Morris, N., R. Rahmani, et al. 2015. A Numerical Model to Study the Role of Surface Textures at Top Dead Center Reversal in the Piston Ring to Cylinder Liner Contact. *J. Tribol.* vol. 138.n. 2, p. 021703.

Qiu, Y. & M. M. Khonsari. 2009. On the Prediction of Cavitation in Dimples Using a Mass-Conservative Algorithm. *ASME, J. of Trib.* vol. 131.n. 4, pp. 041702–1.

Shen, C. & M. M. Khonsari. 2013. On the Magnitude of Cavitation Pressure of Steady-State Lubrication. *Tribol. Lett.* vol. 51.n. 1, pp. 153–160.

Usman, A. & C. W. Park. 2016. Optimizing the tribological performance of textured piston ring-liner contact for reduced frictional losses in SI engine: Warm operating conditions. *Tribol. Int.* vol. 99, pp. 224–236.

Wang, Q. J. & Chung Y. W. 2013. *Encyclopedia of Tribology*. First. Springer.